Experimental study of frictional drag reduction by microbubbles
: Laser measurement and bubble generator

[*]Hisanobu Kawashima, [**]Akiko Fujiwara, [***]Yusuke Saitoh, [***]Koichi Hishida, and [*]Yoshiaki Kodama,

*Center for Smart Control of Turbulence, National Maritime Research Institute,
6-38-1 Shinkawa, Mitaka, Tokyo, 181-0004, Japan
**Department of Mechanical Engineering, The University of Tokyo,
7-3-1 Hongo, Bunkyo-ku, Tokyo 113-8656, Japan
***Department of System Design Engineering, Keio University,
3-14-1 Hiyodhi, Kohoku-ku Yokohamam Kanagawa 223-8522, Japan

To clarify the mechanism of the frictional drag reduction by microbubble, the experimental studies are performed. The optical wall shear stress sensor, an image measurement system for microbubble flow, and a microbubble generator are developed. Firstly, the optical sensor indicates the probability density of Doppler frequency of continuous phase in a microbubble flow shifts to lower frequency side as compared with that of single phase flow. Secondly, it] is shown that the Reynolds stress of the liquid phase in a microbubble flow decreases by using image measurement technique with combination of Particle Tracking Velocimetry, Laser Induced Fluorescence and Infrared Shadow Image technique. Finally, using venturi tube generates the microbubbles. In the present bubble generator, the bubbles expand and shrink rapidly at the pressure recovery region, and tiny bubbles are generated effectively.

1. Introduction

The frictional drag reduction improves a transport efficiency of a long ship because of the most of the total resistance. A number of drag reduction methods such as large-eddy-breaking-up device, polymer, and microbubble technique have been proposed and studied. The microbubble technique is suitable to a large ship like a tanker because injected bubbles to the bow stay near the bottom for a long time.

The drag reduction by microbubble was found by McCormick and Bhattacharyya (1973). Madavan et al. (1984) performed experiments, in which the microbubbles were injected into the turbulent boundary layer in a horizontal channel flow by using porous plate for bubble injection device. They showed that the magnitude of the frictional drag reduction by microbubbles reached up to 80 %. Kodama et al. (2000) tested to the 50 m-long ship with a flat plate bottom, and discussed the local and total skin friction and the effect of the ship length. Kitagawa et al. (2003) showed that a bubble deformation in a turbulence shear is likely to decrease a Reynolds shear stress in a flow.

As a measurement of the local wall shear stress, several devices have been used and developed. Yoshino et al. (2004) developed micro hot film wall shear stress sensor for feedback control of wall-turbulent, and improved its dynamic characteristic. Gür and Leehey (1993) developed a new wall shear stress gage measuring by torque acting on the cylindrical body due to the shearing flow of the viscous layer. Wang (1993) developed the wall shear stress sensor based on a porous element by the use of difference of pressure. However, most of these measurements require to calibrate. Moreover, the influence of the bubble accretion to the sensor makes the precise measurement difficult in the microbubble turbulent flow.

In parallel with the skin friction measurement, we have tried many techniques to generate microbubbles. Since generating microbubbles costs energy, it is necessary to control the size of bubbles and their distribution in the boundary layer to achieve an optimized net gain. So far, large numbers of microbubble generation techniques have been investigated. One of the most popular techniques is the utilization of gas-liquid instability, for example swirling jet nozzle with bubble injector (Onari, 1997), static mixer and air nozzle surrounded by liquid jet nozzles (Martinez-Bazan et al., 1999, 2000, Takemura and Matsumoto, 2000). Martinez-Bazan et al. (1999, 2000) succeeded in generating the micro-bubbles with less than 50 μm diameter. They revealed that the dissipation rate of the turbulent kinetic energy had strongly correlated to the diameter of generated microbubbles. However, this technique has limitation of the maximum void fraction. The diameter of the generated bubbles becomes larger as increasing void fraction. Bubble forming by decompression of gas-dissolving water is one of the effective techniques to generate small bubbles with the diameter of

20 to 40 μm. Sufficiently aerated water under the high pressure is introduced into the test section, and this gas-dissolving water is decompressed. Since the solubility of air in water is proportional to the pressure, the excess air forms microbubbles. However, the energy to compress the air is required to obtain the high void fraction.

In this investigation the microbubble generator with a converging-diverging nozzle (venturi tube) is proposed. Many researchers have reported the flow structure in converging-diverging nozzle (Toma et al., 1988, Yonechi et al., 1992), and some possibilities of using it as the microbubble generator are denoted. Although the application of venturi cavitation to the microbubble generator is recently suggested by Takemura and Matsumoto (2002), the bubbly flow structure in venturi tube and exact mechanism of bubble breakup are not clear yet. We discuss correlation between flow structure in the nozzle and generated bubble diameter, and the effects of variety of inlet gas flow ratio were discussed to summarize the past achievements.

In this present study, in order to clarify the mechanism of frictional drag reduction by microbubbles, a wall shear stress sensor by optical probe, a measurement system by using image technique with combination of Particle Tracking Velocimetry (PTV), Laser Induced Fluorescence (LIF) and Infrared Shadow Image technique (IST), and microbubble generator by venturi tube are developed. The optical wall shear stress sensor developed by **Yoshino** et al. (2002) for the single phase flow is improved for in microbubble flow. The advanced signal processing for the MEMS senor is implemented in software with a function of size discrimination of tracer particles and bubbles based on the intensity of scattered light signal was added in soft ware after ultra high-speed data aquation. In a combined image measurement system, the effects of the parameters, which are mean velocity in channel, injected air rate, and a measurement position for image measurement, for the drag reduction caused by microbubbles in turbulent flow are investigated.

2. Optical wall shear stress sensor by Laser Gradient Meter (LGM)
2.1 Principle of LGM

To measure the wall shear stress in the near wall region, we applied the optical LGM sensor that was developed by using MEMS techniques. Figure 1 shows a schematic of this sensor principle and Figure 2 shows a probe head of LGM sensor. Linearly diverging interference fringes originate at the surface and extend into the flow. When particles pass through the fringes, they scatter light with a Doppler frequency f that is proportional to the instantaneous velocity and inversely proportional to the fringe separation at the location of particle trajectory. This sensor collects these scattered lights through a receiver at the surface of it like as shown in Figure 1 The local fringe separation d, designed to be linear with the distance from the sensor y, is given

$$d = \kappa \times y \qquad (1)$$

here κ is the fringe divergence rate. And the Doppler frequency that is determined by the velocity of the particle at the any y and the local fringe separation is given

$$f = \frac{u}{\kappa} \qquad (2)$$

where u is the velocity at the any y. The Doppler frequency simply multiplied by the fringe divergence yields the velocity gradient that is equivalent to wall shear stress
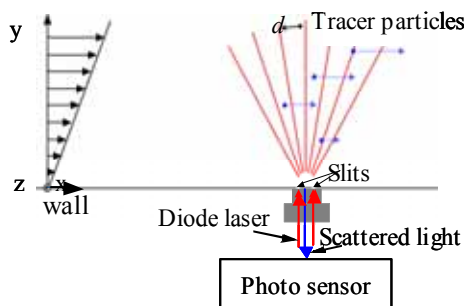
$$\frac{u}{y} = f \times \kappa \qquad (3)$$

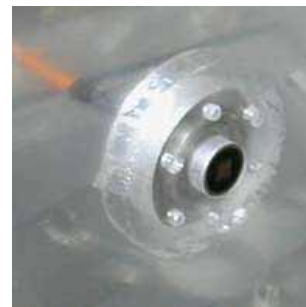Fig. 1 Principle of optical wall shear sensor, which is laser gradient meter (LGM)

Fig. 2 Picture of LGM sensor at a probe head

On the measurement by this sensor, it is a point to notice t Picture of LGM sensor at a probe headhat the probe volume is necessary to be in the linear sub-layer region of the boundary layer, if the velocity gradient is not linear, Equation (2) is not comprise and there is a difference of Doppler signal between upper and under of probe volume. On this sensor 's surface there are two slits at intervals of S=39 μm. Diode lasers with wavelength λ= 660 μm pass through these two slits to originate interference fringes at little way from the surface of sensor head as shown in Figure 3 and in relation to the intersection of the transmitter and receiver field the probe volume is formed at 30 μm and approximately high from the surface of sensor.

In the processing, the time-line data that contained scattered signals was collected by LGM sensor, was amplified by photo multi plier and branched into two ways of signal processing. One is the AC component that is processed with LP filter and HP filter to obtain the Doppler frequency signal, and another is DC component that is processed with LP filter and stands at the intensity of the scattered signal. These two components are stored in the PC through A/D board by 5M sampling rate at the same time. Total record length depends on the memory of A/D board and each component's record length in a single procedure is 15M points.

2.2 Results and discussions

Measurement results in single phase: In this study we measured the near-wall velocity gradient in case from U_c= 0.25 m/s to 3.0 m/s to verify the lowering of Doppler frequency. Each Reynolds number based on a mean velocity is from Re_m= 1340 to 22400. Figure 4 shows a friction coefficient C_f in each case and theoretical value based on Dean's empirical equation

$$C_f = \frac{\tau_w}{0.5\rho U_m^2} = 0.073 \text{Re}_m^{-0.25} \qquad (4)$$

$$\frac{U_c}{U_m} = 1.28 \text{Re}_m^{-0.0116} \qquad (5)$$

and Equation (1)~(3) for calculate the wall shear stress to confirm the validity of the sensor.

Velocity Gradient Measurements in the microbubble flow: To verify the utility of these sensor and signal processing we measure the velocity gradient and Doppler frequency of the scattered lights from bubbles in the turbulent microbubble flow with 1.0 % void fraction. Figure 5 shows the PDF of the Doppler frequency when measured the bubbles' multiple
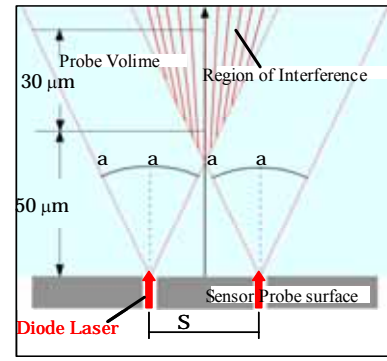
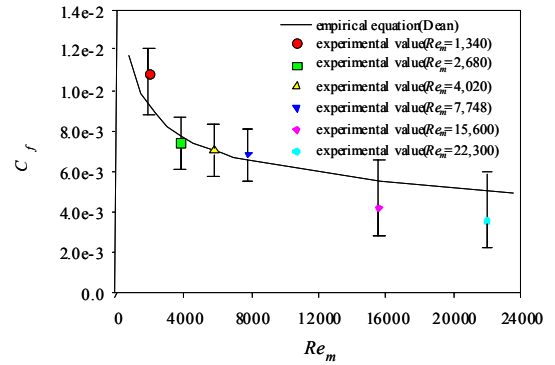Fig. 3 Schematic diagram of Probe volume

Fig. 4 Parallel between experimental friction coefficient and Dean empirical curve
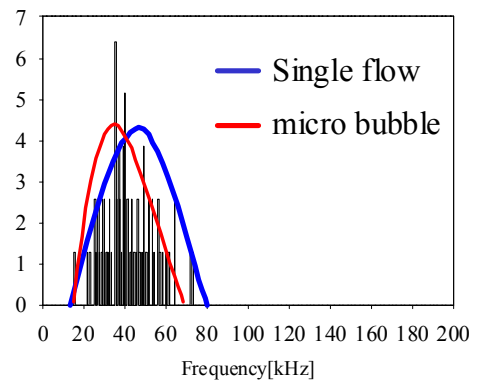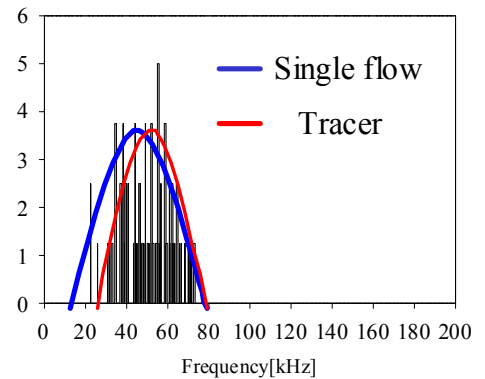
Fig. 5 PDF of Doppler frequency in bubbly flow. Upper graph shows the PDF of single phase flow versus tracer. Lower graph shows the PDF of single phase flow versus a microbubble.

scattered lights without tracer particles. In case of Re_m =7500, PDF shows obviously that the average Doppler frequency is lower than in case of single phase. It suggests that the drag reduction is occurred in probe volume by the effect of bubbles.

3. Horizontal channel

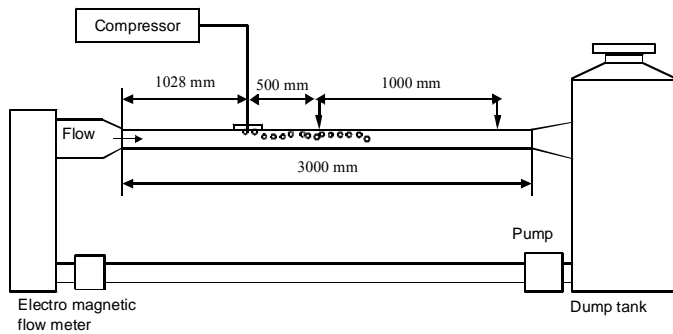### 3.1 Experimental apparatus and conditions

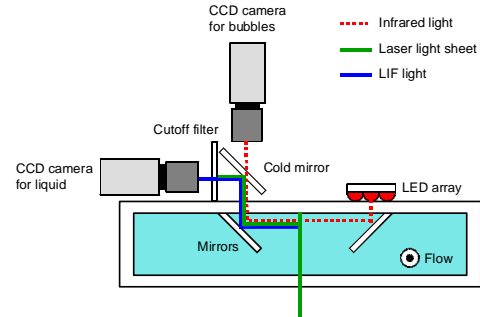Fig. 7 Schematic diagram of an experimental apparatus

Fig. 6 Optical measurement system

Figure 6 shows experimental apparatus for microbubble in an acrylic horizontal channel. It consists of pump, electromagnetic flowmeter, vena contracta, acrylic horizontal channel, which has 3 m for length (L), 20 mm for inner height (H), and 100 mm for inner width (W), and dump tank. A bubble generator device is mounted on the upper wall of acrylic part at 1028 mm from the vena contract. The bubbles are made from compressed air gas through the bubble injector device, which has a slit in 5 mm and 72 mm for width. The mean velocity and air flow rate in a channel are controlled until 10 m/s by a personal computer.

The velocities of the liquid phase and bubbles are measured from captured images by using two cameras, respectively. The image measurement is performed at two positions, where are 0.5 and 1.5 m from bubble generator device, under the conditions which the mean velocities are 5 and 7 m/s, thickness of air (t_a) are 0, 0.15, 0.20 mm. Where thickness air ($t_a = Q_a/(U_m*B_a)$) is defined with a air flow rate (Q_a) divided by a mean velocity (U_m) and a width of the bubble generator (B_a).

Figure 7 shows an optical setup apparatus in cross view of a channel. It consists of two cameras, two light sources (Nd:YAG laser and LED with infrared ray), and mirror system. In the system, two mirrors are located 45 degrees mutually opposite from an upper wall in a channel, a cold mirror separates the laser light and LED light to the different directions, and a cutoff filter is used to divide the lights of laser and scattering light form the fluorescent particles. The visualization area is about 10 mm x 7 mm. The cameras are set the side and above a channel. The optical problems, such as scattering light at the bubble surface and halation at the acrylic channel wall, are avoided by this optical system and an image technique of LIF (Laser Induced Fluorescence).

Nd:YAG laser, which has 532 nm for wavelength, illuminates the fluorescent particles in liquid under the channel. A horizontal CCD camera records the lights from the fluorescent particle through the mirrors in a channel, cold mirror, and cutoff filter. Furthermore, the distribution of velocity in a channel is obtained by using PTV technique (Particle Tracking Velocimetry) from a couple of images. On the other hand, the velocities, sizes, and shapes of bubbles in a channel are recorded by the vertical CCD camera with LED light source, which has an infrared ray of 850 nm for wavelength. Both the cameras and lights are driven by pulse generator and controlled the timing of the pair of the images.

3.2 Results and discussions

Effects of drag reduction by microbubbles: Figure 8 shows the effect of the drag reduction by microbubbles. The horizontal axis means thickness of air, on the other hand, the vertical axis means normalized drag reduction effects (C_f/C_{f0}), which is the coefficient of skin friction in microbubble flow divided by it in single phase flow. The skin friction coefficient is given by,
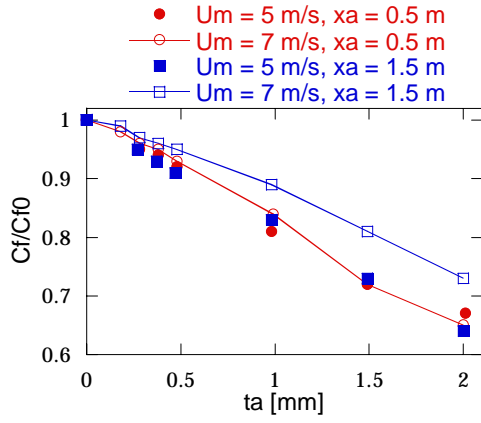
Fig. 8 Ratio of skin friction coefficient in bubbly flow to that single phase flow

Fig. 9 Distribution of the void ratio in a channel

$$C_{f0}(Q_a) = C_{f0}(0)\frac{\tau[U(Q_a)]}{\tau[U(0)]} \qquad (6)$$

, where the $U(Q_a)$ is the mean liquid velocity in microbubble flow, and τ is the wall share stress estimated by the empirical Blasius formula. Furthermore, the symbols means the different experimental conditions: U_m = 5, 7 m/s and measurement position x_a= 0.5, 1.5 m.

As the figure, the lager the effect of drag reduction becomes, the lager the injected air rate in the channel becomes. And when the mean velocity is different, the effect in the slow velocity becomes larger than that in fast at the same position.

Distribution of void ratio in a channel: Figure 9 shows distributions of void ratio in a channel under the condition which the . The horizontal axis shows the void ratio and vertical axis shows the normalized distance ($|y|/h$), which is divided by the half height of a channel, from the acrylic upper wall. The void ratio is defined by the t_B/t_{total}; t_B means that the time of the bubbles through the optical probe, optical probe of 80 micrometer at the tip of it, and t_{total} is the measurement time. The graph shows that the maximum of the void ratio is that $|y|/h$ is from 0.2 to 0.3 in each conditions. For the same velocity, the maximum value of the void ratio at the x_a= 0.5 m becomes lower than that at the 1.5 m and the distribution of the void ratio diffuse until the center of a channel

Fig. 10 Distribution of the Reynolds stress
(U_m=5 m/s, x_a =1.5 m)
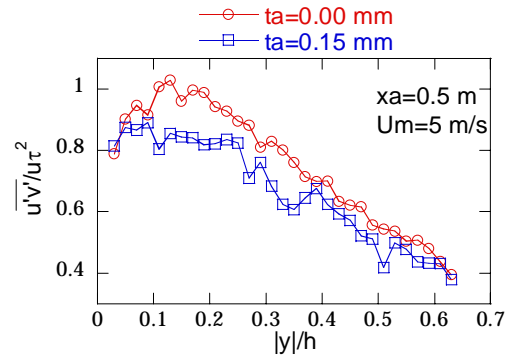
Fig. 11 Distribution of the Reynolds stress
(U_m=5 m/s, x_a =0.5 m)

The Reynolds stress in a channel: Figure 10 and 11 show the distributions of a Reynolds stress of a liquid phase in a channel under the conditions which x_a= 0.5, 1.5 m, U_m = 5 m/s, and t_a= 0.0, 0.15 mm. The horizontal axis shows the normalized distance ($|y|/h$) form the acrylic upper wall. The vertical axis shows the normalized correlation value, which is multiplied by the variations of streamwise (u') and wall-normal direction (v'), divided by the frictional velocity squared (U_τ^2). The figures show that the profile of the Reynolds stress in bubbly flow becomes lower in the whole region in a channel than that case of the single phase flow in spite of the different measurement position. And the amount of a decrease of it tends to increase at position where the normalized distance is between 0.2 and 0.3. This tendency is alike the distribution of the void ratio in a channel, therefore it is clearly shows that the existence of the
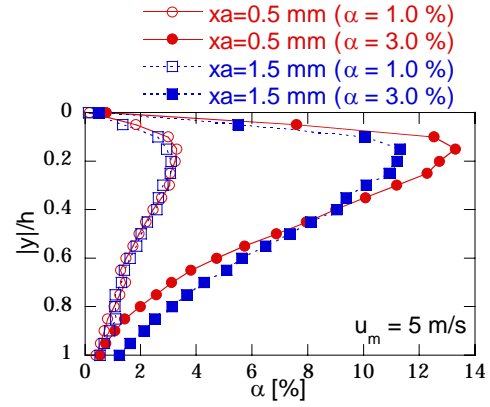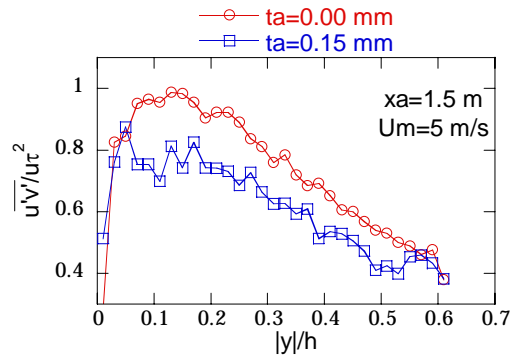
bubble relates to the frictional drag reduction effect. Figure 12 shows the Reynolds stress profile under the condition

which $x_a = 0.5$ m, $U_m = 5, 7$ m/s, and $t_a = 0.15$ mm. The vertical axis ($\overline{u'v'}/\overline{u'_0v'_0}$) is normalized by the Reynolds stress of the single phase flow in each velocity. It is easily see that an amount of the decrease of the Reynolds stress in $U_m = 5$ m/s becomes lager than that in $U_m = 7$ m/s. This result corresponds to the tendency of the drag reduction effects measured by mechanical share stress sensor.

Frequency of the occurrence of negative u'v': Figure 13 shows a sum of the negative of Reynolds stress in a channel ($(u'v')$) divided by U_τ^2 and the frequency of the occurrence of negative $u'v'$ (N_I/N_T), which the N_I is detection number of the sum of negative $u'v'$ and N_T is the total numbe tected $u'v'$ in r of the de a channel. The increasing negative $u'v'$ means the decreasing a Reynolds stress in a turbulent flow and to make the isotropic of the turbulent structure. Therefore it means the frictional drag reduction (Kitagawa et al., 2004). The graph shows that the sum of the Reynolds stresses in a channel decrease with increasing the injected air flow rate in case U_m and x_a are same condition. When the Reynolds stress decreases in each cases, the frequency of the occurrence of negative $u'v'$ increases.

Fig. 12 Distribution of the normalized Reynolds stress

	0.5 m, 5 m/s, ta=0.00 mm
	0.5 m, 5 m/s, ta=0.15 mm
	0.5 m, 5 m/s, ta=0.20 mm
	0.5 m, 7 m/s, ta=0.00 mm
	0.5 m, 7 m/s, ta=0.15 mm
	0.5 m, 7 m/s, ta=0.20 mm
	1.5 m, 5 m/s, ta=0.00 mm
	1.5 m, 5 m/s, ta=0.15 mm
	1.5 m, 7 m/s, ta=0.00 mm
	1.5 m, 7 m/s, ta=0.15 mm
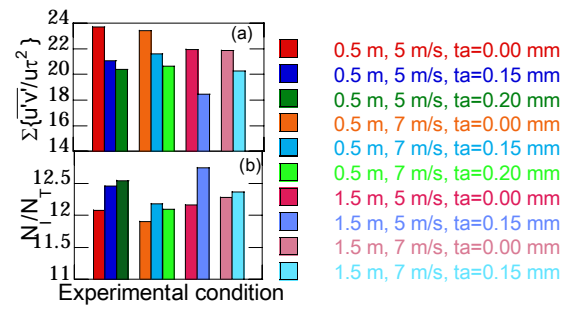
Fig. 13 Sum of negative u'v' and frequency of the occurrence of negative (N_I/N_T),

4. Microbubble generator by venturi tube
4.1 Experimental apparatus and conditions

Figure 14 shows the experimental apparatus consisted of 340 x 340 x 750 mm³ of acrylic tank, a venturi tube, a pump and an air compressor. In order to observe bubble breakup phenomena in the venturi tube, the tube was made of acrylic resin. Figure 14 (b) depicts the venturi tube in detail. Inlet and outlet diameter was 8 mm and the diameter of the throat is 3 mm, that is about 14 % area ratio of the throat to in- and/or outlet. The working fluid was tap water filtered with 5 μm mesh, and it was circulated by the pump. Air was injected from the stainless needle with 0.8 mm inlet diameter. Origin of the coordinate system is defined at the middle of the throat as shown in Figure 14 (b). Downward flow direction is defined as z-axis, and radial direction is defined as r-axis.

The experimental conditions are shown in Table 1. α is inlet gas flow ration under atmospheric pressure which defined by

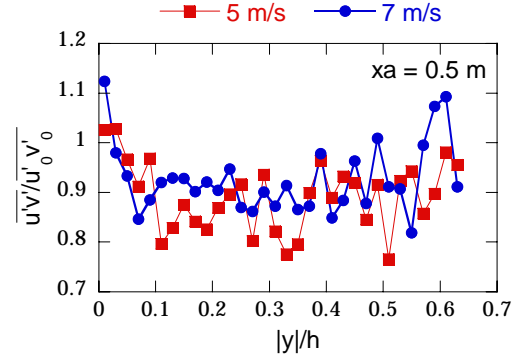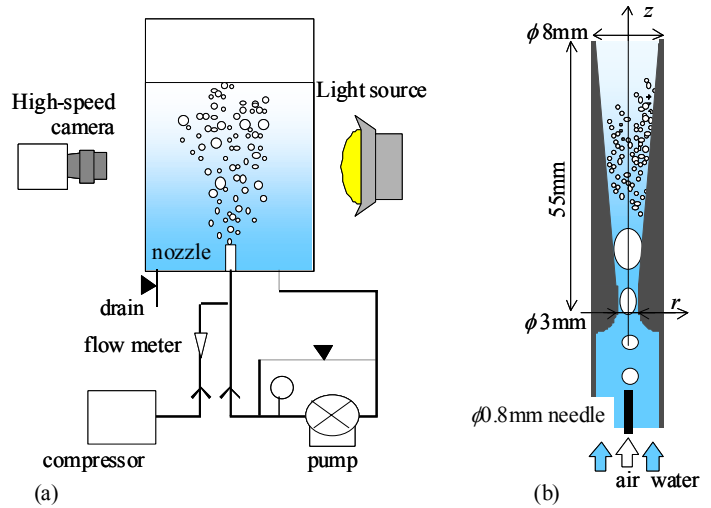$$\alpha = \frac{Q_g}{Q_l + Q_g}, \qquad (7)$$

Fig. 14. Schematic of the experimental apparatus, (a) Experimental setup, (b) Detail of the venturi tube.

Table 1. Experimental conditions.

α [%] :	4, 8, 20,
Q_l [l/min] :	4 ~ 11
u_{th} [m/s] :	9.4 ~ 25.9

(1)

where, Q_g and Q_l are gas and liquid flow rate, respectively. In Table 1, u_{th} is velocity at the throat ($u_{th}=Q_l/A_{th}$, A_{th}: area at the throat). In order to avoid the bubble coalescence for the measurement of bubble diameter right after the fission, 3-pentanol of about 50 ppm was added as the surfactant.

The bubble diameter was measured by projecting technique. As shown in Figure 14 (a), Digital CCD camera (READLAKE MASD, Inc., MotionPro Mono Model1000) was set facing the light source (Phantom Co., Ltd., HVC-SL). Bubble images were captured at about 50~150 mm above the nozzle outlet. The diameter of each bubble was estimated by image-processing technique. In order to evaluate the venturi tube performance as the microbubble generator, Sauter mean diameter D_{32}, which is defined by

$$D_{32} = \frac{\sum_i D_i^3}{\sum_i D_i^2}, \qquad (8)$$

was used. In equation (8), D_i is equivalent diameter of i-th bubble. Sauter mean diameter is one of the effective parameter to evaluate the phenomena strongly affected by surface area.

Figure 15. Probability density distribution of the generated bubble diameter with varied velocity (α=4%).

4.2 Results and discussions

Breakup phenomena in the venturi tube and diameter of the generated microbubbles: Figure 15 corresponds to the probability density distribution of the generated bubble diameter depending on the liquid flow velocity at the gas flow ratio of 4 %. Because of the accuracy of spatial resolution, the profile below 40 μm bubble diameter was not presented. It is shown that there was a different tendency in the case of the velocity of 9.4 m/s, while the other two cases showed similar profiles each other. On the lower liquid velocity condition, bubbles with the diameter of more than 200 m were generated,

Figure16. Typical snapshots of bubble breakup, (a) u_{th}=9.4 m/s, (b) u_{th}=21.2 m/s.

and Sauter mean diamter D_{32} became 360 μm, while on the higher velocity conditions, most of bubbles had the diameter of less than 180 μm, and D_{32} became smaller. Sauter mean diameter became smaller as increasing liquid velocity. The same tendency was identified on the different gas flow ratio conditions. These results suggested that there might be the dominant mechanism of bubble breakup is different depending on the liquid velocity.

Typical snapshots of the bubble breakup in the case of liquid velocity u_{th} with 9.4 and 21.2 m/s were shown in Figure 16. Each figure indicated that the air bubbles from the inlet broke into the small tiny bubbles during the bubbles traveling toward the downstream. On the condition of 9.4 m/s, most of bubbles moved downstream along the nozzle wall, and gas-liquid interface deformed randomly. The ruffles were observed on the surface of air lump at around z of 20 mm. And the tips of the ruffles were broken into small bubbles ($z \sim 30$ mm). These figures suggested that the bubble breakup occurred gradually in the wide region of the diverging area on the lower velocity condition. The ruffles might appear because of the surrounding turbulence flow structure. (Martinez-Bazan et al. (2000)). The effect of turbulence was expected as the one possibility of explaining the dominant mechanism of breakup in the case of the low velocity in the present study.

In the case of high velocity (u_{th} = 21.2 m/s), it seems that tiny bubbles are suddenly generated around 30 mm downstream from the throat in Figure 16 (b). As the red arrow marked, the bubbles went on expanding after passing through the throat. At the certain z position, bubbles shrank rapidly and broke into pieces as the microbubbles. The size
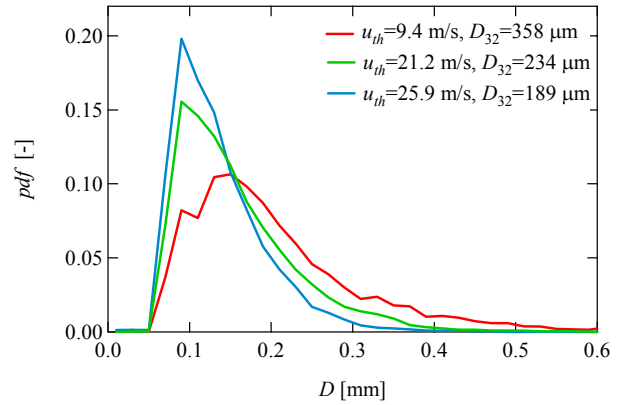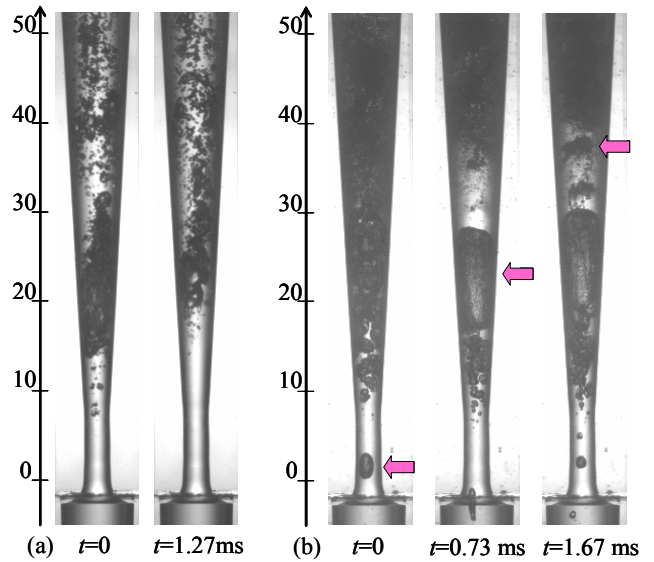
of generated tiny bubbles looked smaller on the higher velocity than that on the lower velocity condition, and it looked like bubble clouds

Flow structure in the ventri tube: In order to discuss the flow structure in the venturi tube, typical pressure distribution in the Laval nozzle is presented in Figure 17. Generally in single phase flow, pressure distribution in the venturi tube is plotted as line *a* to *b* depending on the change of the cross-sectional area. The pressure has minimum value at the throat, and it recovered toward the down stream. In the case of the low velocity, pressure distribution in bubbly flow is expected to be almost same. And bubbles are expected to be broken up into pieces due to the turbulence in the tube as shown in Figure 16 (a).

Pressure at the throat becomes lower with increasing of the velocity (line *a* to *c*). Here, the speed of sound in bubbly flow c_b is estimated by

$$c_b = \sqrt{\frac{p}{\alpha \rho_l (1-\alpha)}}, \qquad (9)$$

where, p is pressure, α is void fraction and ρ_l is liquid density. For instance, the sonic speed c_b becomes nearly 20 m/s in the bubbly flow with void fraction of 20 % in atmospheric condition. This equation indicates that the sonic speed in bubbly flow is much slower than that in single-phase flow (both gas and liquid). Figure 18 depicts estimated speed of sound at the throat in the present venturi tube. It was estimated from the conservation of momentum equation of homogeneous bubbly flow, conservation of mass equation, and state equation of isothermal condition as following.

$$\rho_l (1-\alpha) u \frac{du}{dz} = -\frac{dp}{dx},$$
$$\frac{\rho_g \alpha}{\rho_l (1-\alpha)} = const., and \qquad (10)$$
$$\frac{p}{\rho_g} = const.$$

In Figure 18, u_{th} on each experimental condition are also plotted. In the present study, it suggested that the velocity at the throat became faster than the speed of sound in the case of u_{th} with more than 16 m/s. At that time, the pressure in the nozzle is expected to be decreasing after passing through the throat as shown in Figure 17 (line *a* to *e*). And flow structure is expected to be supersonic field of bubbly flow. In fact, the bubbles were expanded after passing the throat and toward the downstream in Figure 16 (b) ($u_{th} = 21.2$ m/s).
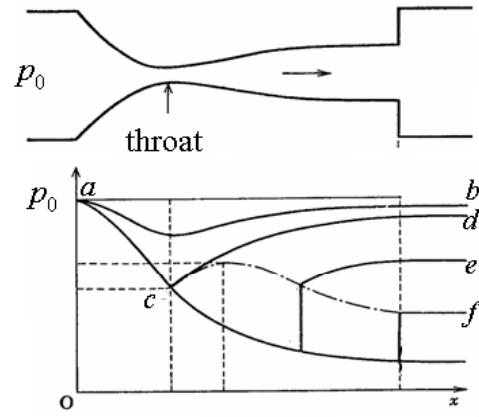

Figure 17. Schematic of typical pressure distribution in Laval nozzle.
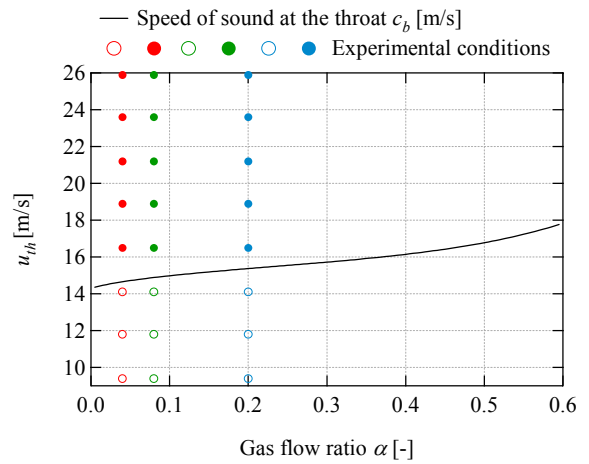

Figure 18. Estimated speed of sound at the throat and experimental conditions.
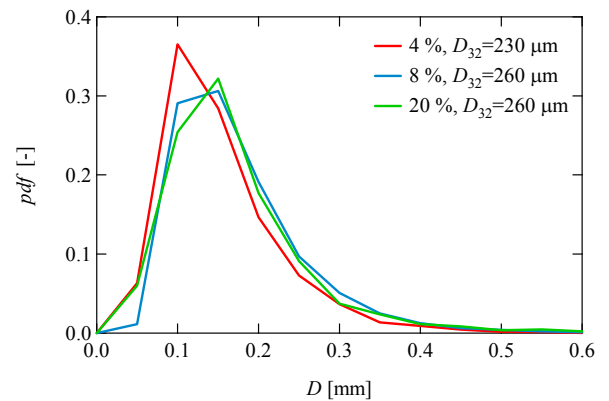

Figure 19. Probability density distribution of generated bubble diameter
with varied gas flow ratio (u_{th} = 16 m/s).

Considering these discussions, it is suggested that on the high velocity condition, the flow structure in the diverging area becomes supersonic field of bubbly flow. Because bubbles are expanded in this are, they shrink rapidly at the

pressure recovery region, and tiny bubbles are generated effectively.

Figure19 shows probability density distribution of bubble diameter with varied gas flow ratio α (u_{th}= 16 m/s). The tendency of distribution and Sauter mean diameter D_{32} were in good agreement with each condition. This result suggested that the present microbubble generator is available for the wide range of gas flow ratio on the condition of the high velocity at the throat.

5. Conclusion

1. We applied a new optical wall shear sensor developed by MEMS techniques for liquid phase in microbubble turbulent flow. A signal processing for micro-bubbly flow has been developed with size discrimination of tracer particles and bubbles based on the intensity of scattered light signal captured by ultra high-speed A/D converter.

2. The results revealed that the signal processing removed the micro bubble scattered signal, and that probability density of Doppler frequency of continuous phase in microbubble flow shifted to lower frequency side as compared with that of single phase flow.

3. A simultaneous measurement system by using image technique with combination of Particle Tracking Velocimetry (PTV), Laser Induced Fluorescence (LIF) and Infrared Shadow Image technique (IST) was applied to microbubble flow in a horizontal channel. The distribution of a Reynolds shear stress $u'v'$ of a liquid in a channel was obtained by using image processing technique under the several experimental conditions, corresponding to mean velocity, injected air flow rate and measurement position.

4. The frequency of the negative $u'v'$ increased, when the Reynolds stress in bubbly flow was smaller than that of the single phase flow.

5. In order to reveal the mechanism of the bubble breakup in the new microbubble generator utilizing converging-diverging nozzle (venturi tube), the detailed observation of the bubble breakup phenomena and measurement of the generated bubble diameter were conducted.

6. It is suggested that on the high velocity condition, the flow structure in the diverging area becomes supersonic field of bubbly flow (similar to Laval nozzle). Because bubbles are expanded in this area, they shrink rapidly at the pressure recovery region, and tiny bubbles are generated effectively.

7. The present microbubble generator is available for the wide range of gas flow ratio on the condition of the high velocity at the throat.

Reference

Kitagawa, A., Sugiyama, K., Ashihara, M., Hishida, K., and Kodama, A., 2003, "Measurement of turbulence modification by microbubbles causing frictional drag reduction," 4th ASME/FED and JSME joint Fluids Conf. #FEDSM2003-45648 (CD-ROM).

Kitagawa, A., Hishida, K., Kodama, Y., 2004, "Turbulence Structures of Microbubble Flow Measured by PTV/LIF/SIT," Proceedings of 5th Int. Conf. on Multiphase Flow, ICMF-2004, pp.39, Paper No.521 (CD-ROM).

Kodama, Y., Kakugawa, A., Takahashi, T., Kawashima, H., 2000, "Experimental study on microbubbles and their applicability to ships for skin friction reduction", Int. J. Head and Fluid Flow, vol. 21, pp. 582 – 588.

McCormick, M.E. and Bhattacharyya, R., 1973, "Drag Reduction of a Submersible Hull by Electrolysis", Nav. Eng. J., vol. 85, pp. 11–16.

Madavan, N.K., Deutstu, S., and Merkle, C.L., 1984, "Reduction of turbulent skin friction by microbubbles," Phys. Fluid, vol. 27, pp. 356–363.

Martinez-Bazan, C., Montanes, J.L., Lasheras, J.C., 1999, "On the breakup of an air bubble injected into a fully developed turbulent flow. Part 1. Breakup frequency", *J. Fluid Mechanics*, Vol. 401, pp.157-182.

Martinez-Bazan, C., Montanes, J.L., Lasheras, J.C., 2000, "Bubble size distribution resulting from the breakup of an air cavity injected in to a turbulent water jet", *Phys. of Fluids*, Vol. 12 No. 1, pp.145-148.

Gharib M., Modarress D., Fourgutte D., and Wilson D., 2002, "Optical Microsensors for Fluid Flow Diagnostics," 40th AIAA Aerospace Science Meeting &Exhibit, Reno, NV., # AIAA 2002-0252.

Onari, H., 1997, "Waste water purification in wide water area by use of micro-bubble techniques", *Japanese j. Multiphase Flow*, **11**, 3, pp.263-266 (Japanese).

Takemura and Matsumoto, Japanese Patent: number 2000-392677.

Takemura and Matsumoto, Japanese Patent: number 2002-031542.

Toma, T., Yoshino, K., Morioka, S., 1988, "Fluctuation characteristics of bubbly liquid flow in converging-diverging nozzle", *Fluid Dunamics Research*, 2, pp.217-228/

Yoshino, T., Suzuki Y., Kasagi N. and Kamiuten, S., 2004, "Optical Thermal Design of Micro Hot-film Wall Shear Sensor," 689. JSME, vol. 70, pp. 38-45.

Y. Gür and P. Leehey, 1993, "A new wall shear stress gauge," Exp. in Fluids, vol. 8, pp. 145-15.

Yonechi, H., Suzuki, M., Ishii, R., Morioka, S.,1992, "Bubbly flows through a convergent-divergent nozzle", *Mem. Fac. Eng., Kyoto Univ.*, Vol.54 No.2, pp. 83-104.

Z. Y. Wang, 1993, "Experimental study of a wall shear stress sensor based on a porous element," Exp. in Fluids, vol. 14, pp. 153-157.